Development of structured illumination microscope using transmission diffraction grating obtained by analogue microfilming method

Aleksa Denčevski[1], Jovana Z. Jelić[1], Ana Senkić[2], Aleksandar Krmpot[1], and Mihailo D. Rabasović[1]

[1]Univerzitet u Beogradu Institut za Fiziku
[2]Institute of Physics Zagreb

May 26, 2024

Abstract

We present the development of a custom-built structured illumination microscope (SIM) featuring a specially designed transmission diffraction grating. Employing the analogue microfilming method, we fabricated transmission diffraction gratings suited to the specific requirements of our system. This robust and cost-effective method allows for the fabrication of diffraction gratings with customised constants, ensuring excellent transmission in both the visible and near-infrared spectra. Additionally, to assess the performance of our system, we measured the resolution in both epifluorescent and superresolution imaging modalities by applying two independent methods: the conventional resolution measurement using fluorescent beads and the knife-edge technique applied on the MoS $_2$ monolayer flakes. Both methods confirmed enhancement in the resolution of SIM over the epifluorescent imaging modality. Furthermore, we have successfully demonstrated the capabilities of our microscope by imaging fluorescently labelled astrocytes, specifically targeting the vimentin filament protein within these cells. The superresolution images reveal fine structures of the vimentin cytoskeleton that remain unresolved in the epifluorescent image.

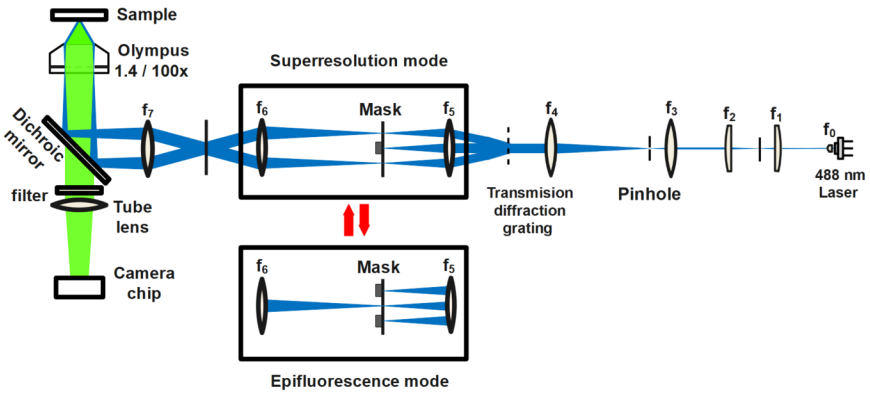

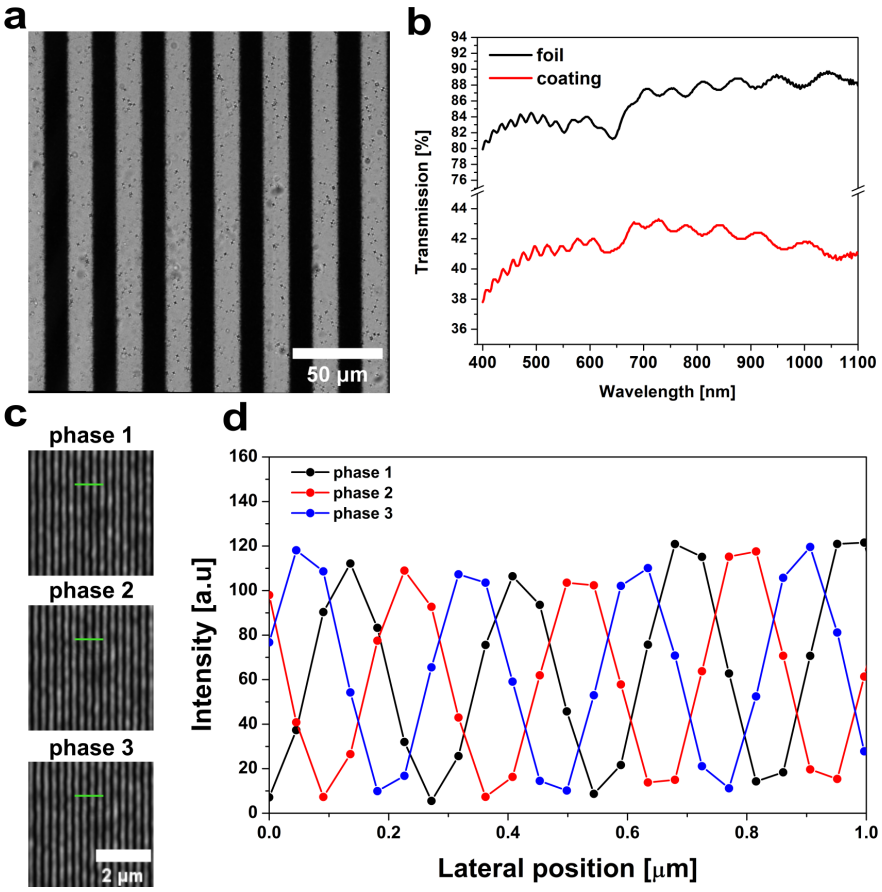

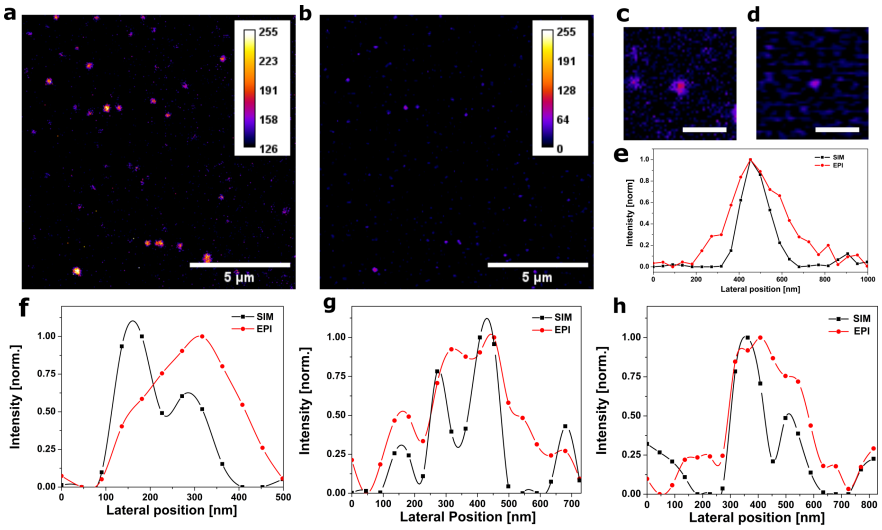

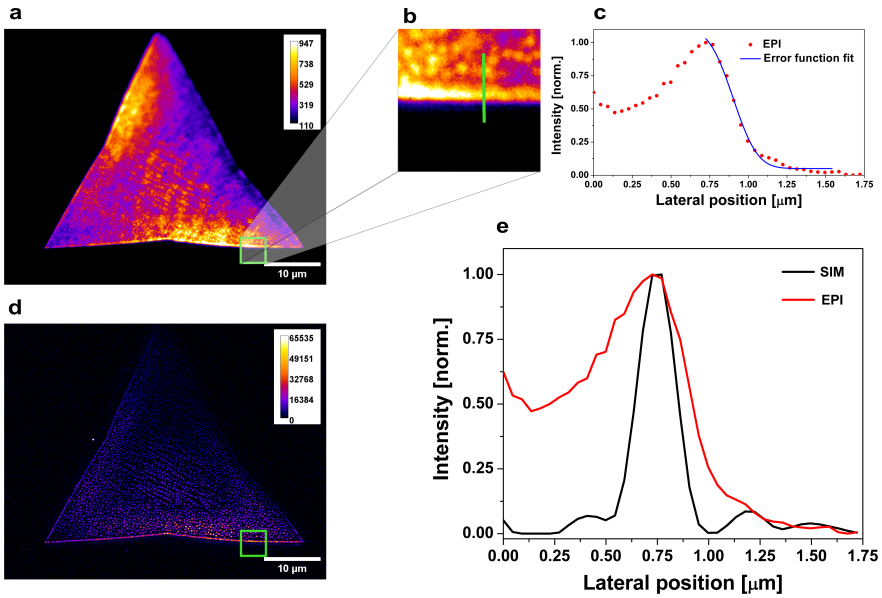

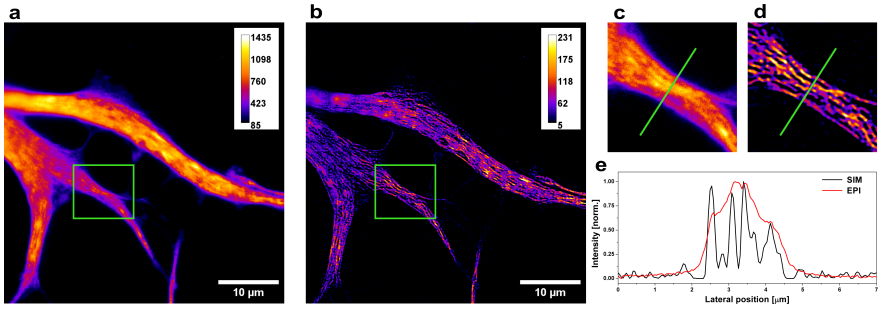

Development of structured illumination microscope using transmission diffraction grating obtained by analogue microfilming method

Aleksa Denčevski[1], Jovana Z. Jelić[1], Ana Senkić[2], Aleksandar J. Krmpot[1], and Mihailo D. Rabasović[1]

[1]Institute of Physics Belgrade, University of Belgrade, National Institute of the Republic of Serbia, Pregrevica 118, 11080, Belgrade, Serbia
[2]Centre for Advanced Laser Techniques, Institute of Physics Zagreb, Bijenička cesta 46, 10000, Zagreb, Croatia

Abstract

We present the development of a custom-built structured illumination microscope (SIM) featuring a specially designed transmission diffraction grating. Employing the analogue microfilming method, we fabricated transmission diffraction gratings suited to the specific requirements of our system. This robust and cost-effective method allows for the fabrication of diffraction gratings with customised constants, ensuring excellent transmission in both the visible and near-infrared spectra. Additionally, to assess the performance of our system, we measured the resolution in both epifluorescent and superresolution imaging modalities by applying two independent methods: the conventional resolution measurement using fluorescent beads and the knife-edge technique applied on the MoS_2 monolayer flakes. Both methods confirmed enhancement in the resolution of SIM over the epifluorescent imaging modality. Furthermore, we have successfully demonstrated the capabilities of our microscope by imaging fluorescently labelled astrocytes, specifically targeting the vimentin filament protein within these cells. The superresolution images reveal fine structures of the vimentin cytoskeleton that remain unresolved in the epifluorescent image.

Keywords: super-resolution microscopy, structured illumination microscopy, diffraction grating, resolution measurement

1 Introduction

Fluorescent microscopy is one of the most widely used methods for the visualization of biological samples. However, its resolution is fundamentally limited by diffraction. The diffraction limit, commonly defined by Abbe or Rayleigh criteria, depends on the excitation wavelength and numerical aperture of the objective lens, [1]. In recent years, novel methods have been developed to exceed the diffraction limit and enable the recording of the fine structures of biological samples [2], [3], [4]. Among these techniques, a simple optical configuration of structure illumination microscope emerged as a powerful approach that enables the enhancement of resolution up to two times compared to the diffraction limit,[5], [6], [7], [8].

All SIM setups utilize a regular illumination pattern to excite fluorescent samples. Microscopes might be regarded as low-pass spatial frequency filters. Specifically, the pattern enables the inclusion of high-frequency components of the sample structure within the frequency range that can be recorded. By recording multiple images at various angles and phases of the pattern, it becomes possible to achieve an image resolution surpassing the diffraction limit by reconstruction, [5].

Several methods have been developed for generating the illumination pattern in SIM. Commonly, diffraction gratings are employed to generate the pattern on the sample, whereas two diffraction orders interfere in the focal plane of the objective [9], [10], [11], [12],[13]. In many applications, the beam is shaped using diffractive optical elements (DOE) [14], a spatial light modulator (SLM) [15], or a digital micromirror device (DMD) [16, 17]. The fiber coupler method has also been utilized to generate two [18] or three beams [19, 20] that interfere in the sample plane, effectively producing the pattern. While these approaches allow for the rapid generation of complex patterns, they are considerably more expensive and technically challenging compared to the use of diffraction gratings.

To surpass the diffraction limit and achieve higher-resolution imaging, it is necessary to perform reconstruction using the recorded images and remove the pattern generated by any of the aforementioned methods. Various software tools have been developed for image reconstruction, with notable examples including FairSIM [21] and SIMToolBox [22, 23]. In recent years, novel software solutions have emerged to enable image reconstruction using only three recorded images without changing the pattern phase [24, 25]. On the other hand, applications utilizing three-beam interference allow for sample recording without pattern rotation [20, 26, 27].

In this study, we will present the development of a custom-built SIM microscope as well as the measurement of the resolution of two imaging modalities by several independent methods. Also, we will present the recording of biological samples to present the capabilities of our custom-built setup.

Due to critical limitations with commercially available options, we have developed a method for the fabrication of transmission diffraction gratings suited to the specific requirements of our system. The primary drawback of commercial gratings for SIM setups is the lack of symmetry in optical power distribution between diffraction orders. The power of the first diffraction order predominates over the power of higher orders. On the contrary, the developed method enabled us to fabricate diffraction gratings with prefere constants, suitable for both visible and near-infrared spectra. Also, we developed a mechanism for rotating the

diffraction grating and adjusting its position. By rotating the grating just three times and changing the phase three times, we can record nine images for subsequent reconstruction.

Our system allows for imaging in both epifluorescent (EPI) and superresolution (SIM) modalities using a single setup, facilitated by a rapid and straightforward mode-switching mechanism. To minimize sample exposure to laser radiation, the entire system is hardware-trigger-controlled. We have implemented an Arduino microcontroller for easy synchronization and activation of all system components.

For data analysis, we employed the OS-SIM and MAP-SIM algorithms from the SIMToolbox software, an open-source tool available at [28]. To control the entire system, we have developed user-friendly software that not only enables simple operation but also ensures reliable and selective data storage.

2 Methods

2.1 2D SIM setup

We have built a custom-made 2D SIM, Figure 1, based on the arrangement presented in [6]. The mechanical foundation of our system is provided by a microscopic frame (ICM405, Zeiss, Germany), from which the original optical components were removed. Through the meticulous design of mechanical elements, we reconfigured the microscopic frame and positioned optical components such as the dichroic mirror (DM) and tube lenses (TL) in both excitation and emission, aligning them according to the requirements of our system.

For the excitation, a laser diode (SHD4850MG, Roithner Lasertechnik GmbH, Austria) at 488 nm is used, providing an elliptical beam with a maximum output power of 50 mW. Laser diode current and power levels are controlled by a laser driver (LDC205C, Thorlabs, USA). Ellipticity correction is achieved using a beam expander (BE) with two cylindrical lenses (f_1, f_2). A second BE, consisting of two plano-convex lenses (f_3, f_4), is employed for beam expansion. Since the laser diode operates in a multimodal transversal mode, a 30 μm pinhole is positioned at the common focal plane of the lens (f_3) and (f_4) for additional spatial filtering. The absence of higher mode artefacts is confirmed by measuring the beam profile before and after correction. Power losses of approximately 20% are attributed to spatial beam filtering.

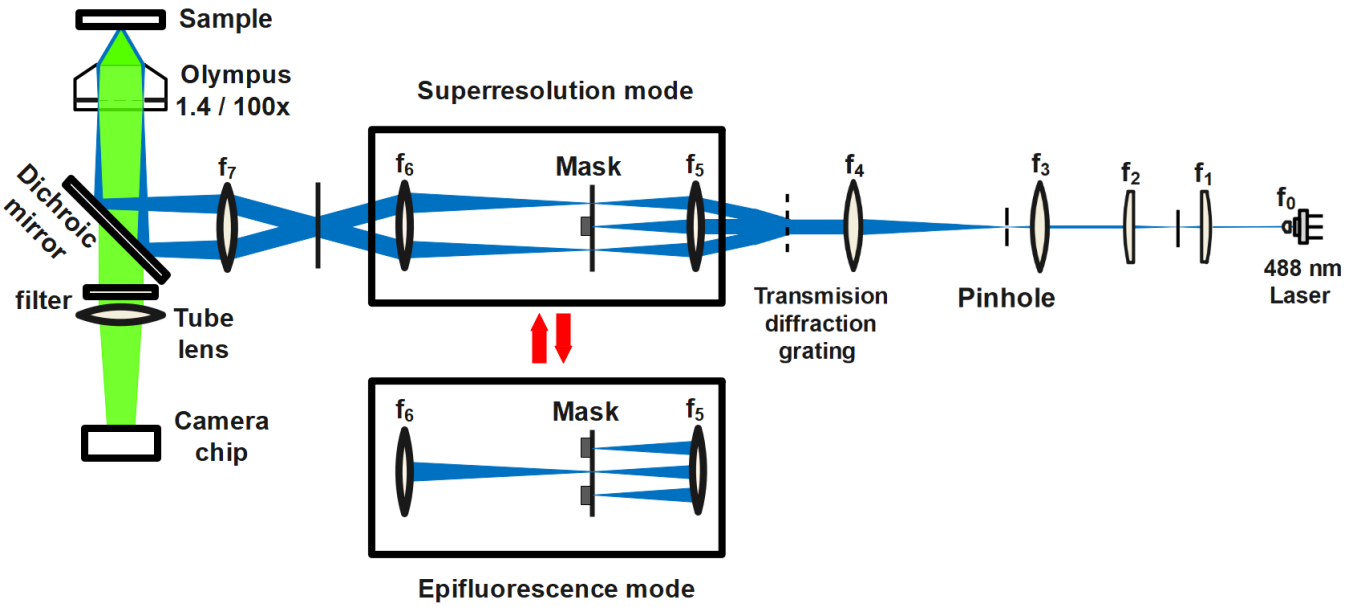

Figure 1: **2D SIM experimental setup.** A laser diode at a wavelength of 488 nm is used for excitation. A system consisting of two BEs and a pinhole aperture is used for beam cleaning and expansion, enabling the expanded beam to reach the diffraction grating. In the EPI imaging modality, all orders except zero are cut off. In the superresolution SIM imaging modality, only ± 1 diffraction orders are allowed to pass. We use this mode to record images for subsequent reconstruction. The fluorescent signal passes through an objective lens, a dichroic mirror, and an emission filter before being focused onto the camera chip using a tube lens.

The collimated and filtered beam is directed onto a specially developed transmission diffraction grating with a constant of 40.1 μm. The properties and design of the diffraction grating are discussed in detail in chapter 3.1. The diffraction grating is mounted on a rotational-translational stage, originally designed according to [29]. This grating can be rotated by the preferred angle in the plane perpendicular to the direction of beam propagation. The stage also facilitates precise translation movement of the grating, allowing for control of the phase of the illumination pattern in the focal plane of the objective. Details of this precision stage are described in the next chapter. The grating is positioned in the focal plane of the lens (f_5), which, together with the next lens (f_6), forms a BE with an expansion factor of 1.5. The BE enables the use of a somewhat coarser diffraction grating, significantly facilitating its production, while also allowing for more precise control of the pattern's phase change.

A mode-switching mechanism consisting of two masks mounted on a specially designed turret is positioned in the plane of the lens (f_5). This setup allows for operation in two distinct modes: epifluorescent and super-resolution. The first mask selectively filters out all orders except the zero-order, facilitating work in epifluorescent mode. The second mask blocks all orders except -1 and 1, providing structured illumination in super-resolution mode. A mode-switching mechanism ensures consistent positioning for efficient order filtering and a smooth transition between microscope operating modes.

Following this beam expansion, the beam(s) is (are) directed onto the TL (f_7), an achromatic lens with a focal length of 200 mm. Importantly, the focal plane of the TL aligns with the back focal plane of the objective. The entire optical system is designed to complement the objective (UPLSAPO100XO/1.4, Olympus, Japan). In the super-resolution mode, the -1 and 1 diffraction orders reach the edges of the back aperture, achieving the finest pattern in the sample plane with a pattern period of 272 nm.

The aforementioned DM (DMLP490R, Thorlabs, USA) was used to separate the excitation light from the emission light. The emission branch of our setup is designed to incorporate as few optical components as possible to minimize the losses in the fluorescence signal. Fluorescence collected by the objective is directed onto a DM and a TL (TTL 200, Throlabs, USA). For detection, we use a camera (CS2100M - USB, Thorlabs, USA) mounted on a translational stage, enabling precise adjustment of its position along the optical axis. The camera features a chip with dimensions of 1920×1080 pixels and a pixel size of 5.04 μm. Each pixel on the camera corresponds to an area of 45.3 nm $\times$ 45.3 nm in the sample plane. Spectral filtering is implemented in both the excitation (FELH0500, Thorlabs, USA) and emission (MF530-43, Thorlabs, USA) arms.

2.2 Control System

The board (TSI-IOBOB2, Thorlabs, USA) functions as a shield for the Arduino microcontroller and monitors the camera's activity. It enables the triggering of the camera by detecting either the rising or falling edge of the trigger signal. Stepper motors (NEMA 17, Stepperonline), controlled via a driver (TB6600, Stepperonline), handle the rotation and translation of the diffraction grating. The system is synchronized so that the laser diode is active only during the camera exposure. The rotation of the diffraction grating and pattern's phase shift take place only when the laser diode is turned off to reduce the phototoxicity and photobleaching of biological samples.

The entire setup is controlled using user-friendly software developed in the Python programming language. The software enables the selection of parameters such as the rotation angle of the diffraction grating, the number of phases, and the exposure time. It provides precise control of the laser diode power levels using the digital-to-analogue converter, directly controlled by the same microcontroller. Moreover, the control software allows for a seamless selection of operating modes for a rapid transition between epifluorescent and superresolution imaging modalities. The software automatically generates appropriate folders to store recorded images and important information regarding measurement conditions, such as laser power, camera exposure time, objective type, and the size of the field of view.

2.3 Image Reconstruction Software

The recorded images were used for reconstruction using the open-source software SIM-Toolbox [28] which offers a range of algorithms for image reconstruction. Specifically, we employed two algorithms: OS-SIM, which allows for the resolution improvement up to a maximum of 1.4 times [30], and MAP-SIM, capable of potentially reducing artefacts caused by refractive index miss-matching within the samples and illumination imperfections. We opted for this software due to its ability for manual recognition of peaks in Fourier space using

different filters. While reconstruction typically involves a calibration file [28], our developed setup does not support such calibration.

3 Results

3.1 Fabrication and characterization of diffraction gratings

The core component of the SIM setup is the system responsible for generating an interference pattern in the sample plane. This system features a specially designed diffraction grating mounted on a stage, facilitating both translational and rotational motion of the grating. This capability allows for precise manipulation of the interference pattern within the sample plane. We fabricated transmission diffraction gratings using the microfilming method [31]. Initially, a grating pattern generated by a matrix of pixels was printed. The size of this matrix was determined by the dimensions of the paper used for printing and the printing resolution. Specifically, we utilized 300 mm $\times$ 200 mm photo matte paper with a printing resolution of 300 dpi, resulting in a matrix of 3452 rows by 2362 columns. Subsequently, we populated the matrix with zeros and units, where a unit represented a black-coloured pixel on the paper, and a zero indicated transparent pixel. We ensured that each row of the matrix contained alternating segments of zeros and units, maintaining an equal width of transparent and non-transparent stripes in the grating. By comparing the paper size to the number of pixels, we determined the printed grating pixel size to be approximately 85 μm $\times$ 85 μm. We obtained printed gratings with constants ranging from 170 μm to 2040 μm. Subsequently, we used an analogue microfilming device, with a maximum scanning resolution of 640 dpi. The resulting transmission diffraction gratings are 10 mm wide and have a constant ranging from 13.3 μm to 89.5 μm. The resolution of the microfilming device limits the finest possible diffraction grating constant we can achieve. The finest usable diffraction grating we generated has a constant of 13.3 μm.

Additionally, we determined the constant of each obtained diffraction grating using two approaches. Firstly, we recorded the bright-field images of the diffraction gratings with our microscope, Figure 2a. The grating constants were then calculated using these images and the prior knowledge of the pixel size. The second method involved conventional measurement of the position of diffraction orders. Both methods gave identical results.

Furthermore, we examined the transmission properties of the foil used for microfilming, as well as the transmission characteristics of the coating. The transmission curves, Figure 2b), clearly illustrate certain losses on the foil material. However, diffraction gratings fabricated in this manner can be used in both the visible and near-infrared parts of the spectrum. Even though the analogue microfilming method is known as a permanent method for data storage, there is a lack of information regarding the potential effects of the high-intensity radiation on the microfilm foil, to the best of our knowledge. Hence, we investigated the photostability of the produced gratings through regular usage over a two-year timeframe. The average power density applied to the diffraction grating was approximately 0.2 Wcm^{-2}. Our observations revealed no degradation of the grating over time.

In addition to the appropriate diffraction grating constant, the second requirement for SIM grating is to have a symmetrical power distribution between ± 1 orders to achieve

high contrast. We measured the power distribution across different orders and confirmed that the variation in power distribution between ±1 orders is approximately 5% or less. Table 1 provides an overview of the produced transmission diffraction gratings, outlining the constants of the printed gratings used in the production of corresponding diffraction gratings, as well as the power distribution between ±1 and 0 diffraction orders relative to laser power measured immediately after the diffraction grating.

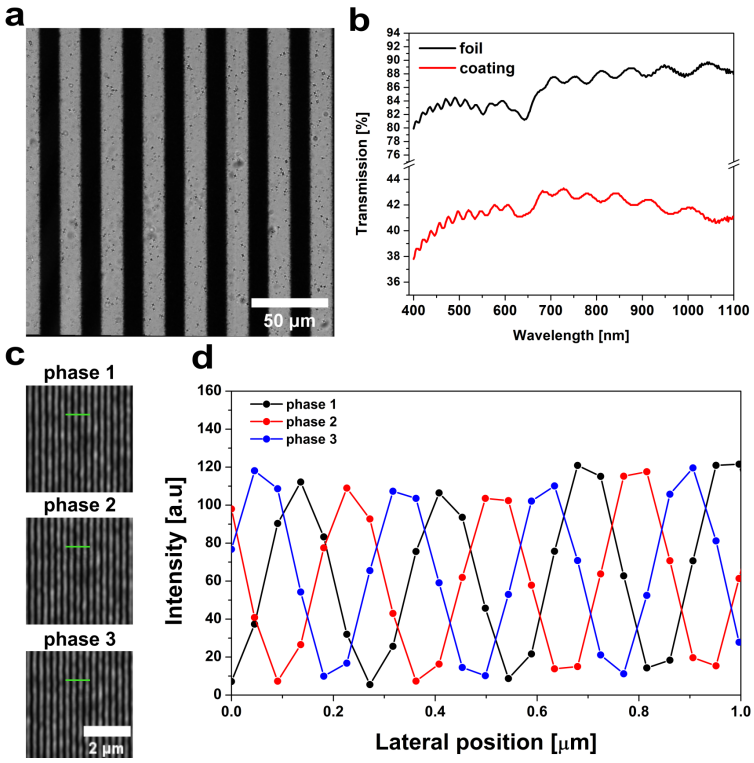

Figure 2: **Illustration of diffraction grating characteristics and phase control.** a) Bright-field image of the transmission diffraction grating. b) Transmission of both the microfilm foil and coating. c) The interference patterns in the sample plane shifted by one-third of the diffraction grating constant were recorded as a demonstration of phase control. d) The intensity profiles extracted at the marked position (green line) on the corresponding interference patterns.

Table 1 indicates specific losses associated with each grating, all of which remain below 20%. These losses result from the presence of higher diffraction orders, which occur due to the non-sinusoidal transmission of the grating. This limitation is inherent to the analogue microfilming method. The presence of higher diffraction orders does not affect the interference image due to the implementation of a mask. This mask effectively removes the higher diffraction orders, ensuring a rapid transition between microscope imaging modalities.

To facilitate adjustments in both the pattern phase and rotation angle, we developed a specialized mechanical translational-rotation system. This system involves securing the mount of the transmission diffraction grating to a timing pulley, enabling rotation around a free axis. This arrangement enables the rotation of the grating in a plane perpendicular

Matrix's period [pixel]	Printed grating constant [μm]	Diffraction grating constant [μm]	P_{-1} [%]	P_0 [%]	P_{+1} [%]
4	340	13.3	18	44	19
6	510	22.5	19	44	17
8	680	27.4	19	44	19
10	850	33.9	24	43	24
12	1020	40.1	23	41	23
14	1190	47.9	22	41	22
16	1360	54.2	24	43	24
18	1530	61.4	22	43	21

Table 1: **Overview of produced transmission diffraction gratings.** The matrices employed to fabricate these gratings had varying periods, resulting in a range of constants for both printed and microfilmed versions. Additionally, the table outlines the power distribution among the zeroth, ± 1 orders of diffraction, offering insights into the performance of the gratings.

to the direction of laser beam propagation. The aforementioned timing pulley is linked to a smaller pulley via a timing belt. The smaller pulley is then linked to the axis of a stepper motor, which is controlled via a driver. The reduction ratio between these two timing pulleys allows for a rotation of the grating by 120° when the motor axis completes a 360° rotation. Therefore, our system operates independently of the driver's micro-stepping. The entire assembly is mounted on a differential translator, similarly controlled by a stepper motor-driver setup. This arrangement ensures the consistent rotation of the diffraction grating and adjustment of the phase for the preferred displacement. Typically, the diffraction grating is shifted by an nth fraction of the grating constant. In our setup, we commonly rotate the grating by 120° and shift the diffraction grating three times by a third of the grating constant. However, this mechanism allows for arbitrary rotation angles and grating displacements as needed.

Given the variety of diffraction gratings produced via the microfilming method, we selected a specific grating where the ± 1 diffraction orders, upon passing through a segment of the optical system, align on the periphery of the back aperture of the objective. This allows for obtaining the finest interference pattern in the sample plane. To investigate the period of the pattern in the sample plane as well as the change in the phase of the pattern, we removed the emission filter and recorded the reflection of the laser. Following this, we analyzed the intensity profiles extracted from the resulting interference images and determined the distance between the maxima of the pattern perpendicular to its propagation. Based on the prior knowledge of the camera's pixel size in the sample plane, we determined the pattern's period to be 272 nm.

Figure 2c illustrates the variations in the interference pattern as the diffraction grating undergoes controlled translation. Additionally, Figure 2d shows the intensity distribution of the interference pattern for one angle of the diffraction grating and three different phases. The interference pattern is clearly shifted by one-third of a grating constant. To ensure that

the grating shifts by the nth part of the grating constant, we first determined the number of stepper motor steps required to move the grating for the grating constant. This allowed us to establish the relationship between the rotation of the stepper motor and the phase of the pattern. This information helped us determine the number of steps needed to shift the grating when positioned at an arbitrary angle relative to the direction of motion of the differential translator used for phase shifting. The same interference image was used to investigate the rotation of diffraction grating. Consecutive images of grating rotated by 120° were recorded. A fast Fourier transform (FFT) of all images was performed and the rotation angle was compared to the software-selected rotation angle. A deviation of 0.2° was observed after three consecutive rotations of the diffraction grating by 120°. This information was used for correction in the software. Additionally, we examined potential deviations in both the direction and speed of rotation of the motor, but no significant deviations were observed. Calibration of the pattern's phase and correction for deviations in the position of the diffraction grating during rotation are key components of the control system we developed.

3.2 Assessment of the SIM resolution

The resolution enhancement of SIM over the EPI imaging modality was confirmed through two distinct measurement approaches. Initially, a conventional technique involving the imaging of fluorescent beads was employed. Intensity profiles of individual beads were extracted from the recorded images. Approximately 30 intensity profiles were extracted and fitted with a Gaussian function. The resolution was subsequently determined as the mean value of the FWHM values obtained from the processed intensity profiles.

Secondly, we applied the knife-edge technique on transition-metal dichalcogenides, specifically on MoS_2 monolayer flakes. Due to their sub-nanometer thickness [32], MoS_2 monolayer flakes provide sharp edges suitable for resolution measurements using the knife-edge technique [33]. Intensity profiles over the edge of the monolayer flake were extracted at approximately 30 positions along the edge and then fitted with the error function (which represents the integral of a Gaussian function). As in the conventional technique, the resolution was calculated as the mean of the FWHM parameters obtained from the processed intensity profiles. These procedures were performed for both EPI and SIM imaging modalities.

3.2.1 Conventional Resolution Assessment

For conventional resolution measurement, we used the TetraSpeck Fluorescent Microspheres Size Kit (Invitrogen, Thermo Fisher Scientific). This kit contains fluorescent microspheres, often referred to as beads, arranged in six viewing regions on a single microscopic slide. Each region contains beads of specific nominal sizes: 0.1 μm, 0.2 μm, 0.5 μm, 1.0 μm, or 4.0 μm, as well as a mixture of all sizes. For our resolution measurements, we specifically used the 0.1 μm beads. Each bead is fluorescently labelled with four distinct fluorescent dyes, one of which corresponds to excitation at the wavelength of 488 nm. For spectral filtering, we used a filter (MF530-43, Thorlabs, USA) to complement the emission spectra of the fluorescent label.

First, we recorded an image in EPI modality, Figure 3a. Afterwards, nine images were recorded (for three different phases at each of three distinct orientations of the diffraction

grating) in the SIM modality. The reconstruction performed by the MAP-SIM algorithm of the SIMToolBox software resulted in the SIM image, Figure 3b. The insets, Figures 3c and 3d, show a single bead recorded in the EPI and SIM imaging modalities, respectively. Since the same sample area was imaged in both modalities, intensity profiles were extracted at the same position within the images and compared, Figure 3e. The extracted intensity profiles were further used for resolution assessment. The resolution measurement on the image recorded in EPI mode resulted in a resolution of (243 ± 9) nm. The same procedure applied to the profiles extracted from the SIM image yielded a mean FWHM value of (163 ± 6) nm. The displayed errors represent the errors of the mean. Given the anticipated resolution and bead size, a deconvolution method must be applied for a more accurate resolution measurement.

The systems consisting of two beads at distances comparable to their sizes were observed in different positions within the sample. Figures 3f-h) show intensity distributions of those two-bead systems recorded in both imaging modalities of our microscope. The difference between the continuous intensity distribution extracted from the EPI images and the resolved distribution (according to the Abbe criteria) obtained on the reconstructed SIM images is evident, showing two beads at a distance of approximately 135 nm. A more precise determination of the resolution is limited by the pixelization of the camera [34], with one pixel corresponding to the area of 45.3 nm $\times$ 45.3 nm in the sample plane.

Given that the MAP-SIM reconstruction algorithm depends on two parameters, spectral merging and cut-off, we tested variations in the image reconstruction for different values of these parameters. We used reconstructed images of 0.5 μm fluorescent beads and then extracted the intensity profiles of those beads and fitted them with the Gaussian function. Our objective was to find the parameter values for which we obtained bead sizes smaller than their nominal size value. This process helped us to limit the range of parameter values used for the reconstruction. As for the cut-off parameter, we estimated it based on the FFT of the epifluorescent image recorded before the recording of nine images used for reconstruction.

3.2.2 Resolution Assessment using the knife-edge technique

For resolution assessment using the knife-edge technique, we used MoS_2 monolayer flakes synthesized via the chemical vapour deposition technique, described in detail in [35]. To achieve resolutions approaching the theoretical limit, glycerin was applied on top of the monolayers and secured with a coverglass. Excitation of the sample was performed at a wavelength of 488 nm. The emission filter (FBH 650 - 40, Thorlabs, USA) was used for spectral filtering, as these monolayers exhibit a photoluminescent signal at wavelengths above 600 nm [36]. Initially, we recorded an image of the monolayer flake in EPI imaging modality, Figure 4a. Subsequently, intensity profiles were extracted over the monolayer-substrate boundary, Figure 4b, at approximately 30 positions along the edge of the monolayer flake and then fitted using the error function, Figure 4c. The FWHM parameter of the corresponding Gaussian distribution was determined for each processed intensity profile. The obtained resolution of (212 ± 4) nm in the EPI imaging modality presents the mean value of FWHM values, with the error corresponding to the standard error of the mean.

To determine the resolution in SIM imaging modality, we recorded a set of nine images (for three different phases at each of three distinct orientations of the diffraction grating)

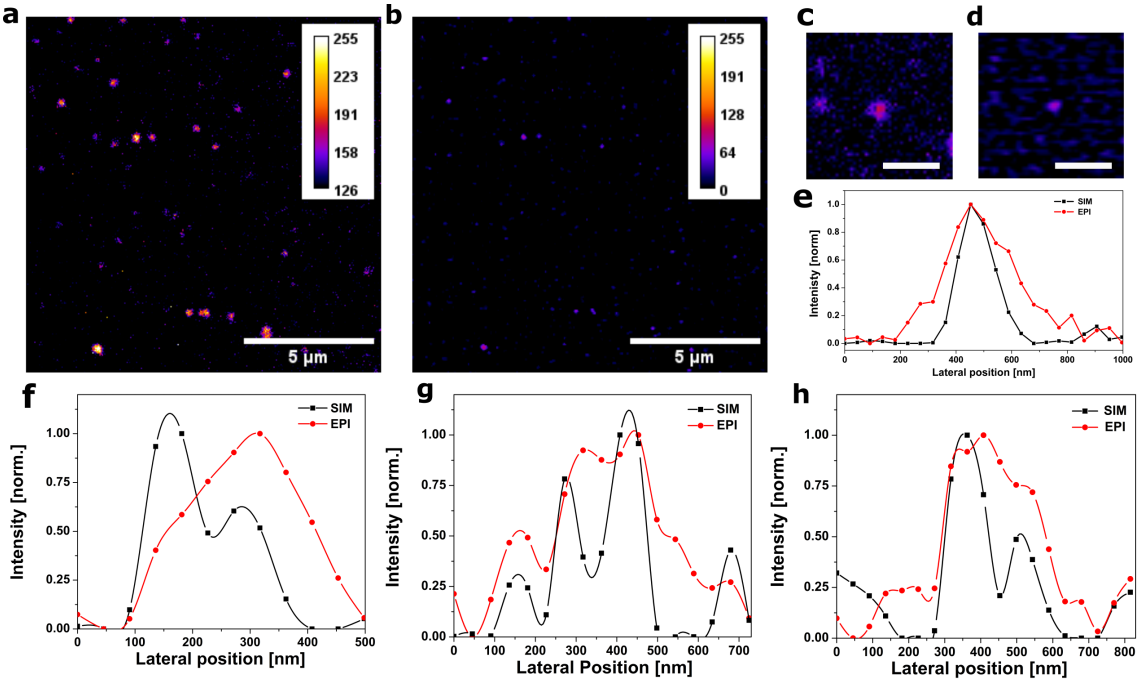

Figure 3: **Conventional resolution measurement technique using 0.1 μm fluorescent beads.** a) The EPI image. b) Reconstructed SIM image obtained by the application of the MAP-SIM algorithm of the SIMToolBox software. The insets show single beads recorded in the EPI c) and SIM d) imaging modalities. Scale bar is 2 μm e) Comparison of single bead intensity profiles extracted from corresponding insets. f-h) Intensity profiles of observed two-bead systems showing continuous distribution in the EPI image and two beads at the distance of around 135 nm, resolved in the reconstructed SIM image.

of the MoS_2 monolayer flake. The reconstructed image, Figure 4d was generated using the MAP-SIM algorithm within the SIMToolBox software. We followed the same data analysis procedures as for EPI imaging to evaluate resolution in SIM modality. The MAP-SIM reconstruction yielded a mean FWHM value of (134 ± 8) nm, indicating an enhanced resolution compared to EPI imaging. The obtained resolution is consistent with the distances between two beads observed in intensity profiles displayed in Figures 3f-h. Furthermore, we investigated the resolution of the image reconstructed by the OS-SIM algorithm. The obtained resolution of (153 ± 5) nm corresponds to the maximum expected improvement of 1.4 times compared to EPI imaging modality [30]. The granulation of the monolayer flake present in the reconstructed image is most likely a consequence of the material growth.

Through the microfilming method, we have successfully developed diffraction gratings capable of generating fine patterns in the sample plane, leading to noticeable improvements in resolution. This enhancement is apparent when comparing the resolution of epifluorescence images with those obtained through superresolution SIM. Moreover, this method allows us to fabricate diffraction gratings with preferred constants, ensuring excellent transmission in both the visible and near-infrared spectra. This versatility enables the development of linear SIM systems for a range of excitation wavelengths, all without significant modifications to the

optical setup. However, there are limitations to consider. Recording using diffraction grating fabricated by the microfilming method is slower compared to SIM setups that utilize SLMs. Also, microfilming only enables the fabrication of black-and-white patterns without grey shades. Nonetheless, the cost-effectiveness of production of these gratings is significantly higher—up to a hundred times—compared to commercial alternatives such as DOE and SLM, [37].

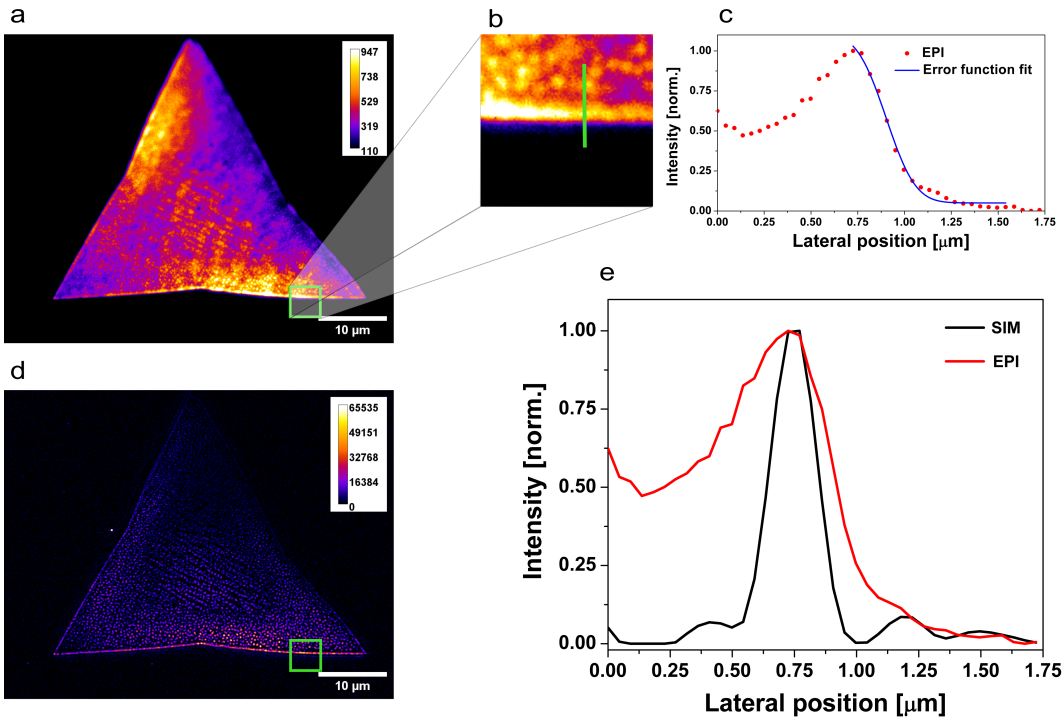

Figure 4: **The application of the knife-edge technique on MoS_2 monolayers.** a) The EPI image of the MoS_2 monolayer flake. b) Shows the extraction of the intensity profile over the edge of the MoS_2 monolayer, followed by fitting using the error function as presented in (c). d) The superresolution SIM image. e) Comparison between the intensity profiles obtained at the marked position of both EPI and SIM images.

The photoluminescent signal obtained from MoS_2 monolayers results in a relatively high signal-to-noise ratio and no-photobleaching effect, making them convenient for the resolution measurement of different microscopic systems. To confirm their photostability, we extracted a 100×100 pixel area within each image from a set of nine images of the monolayer flake and calculated the mean photoluminescent signal intensity. The mean intensity of the signal in this area remains relatively constant, with a maximum deviation of about 5 % across the set of images. Additionally, the sub-nanometer thickness of MoS_2 monolayer flakes [32], makes them suitable for evaluating the quality of the illumination pattern in the sample plane and and for additional system alignment purposes. Furthermore, we investigated if the sample plane is plan-parallel to the diffraction grating's plane by tilting the grating. The observed deviations in the average intensity were over 20 %, confirming that our system was well-aligned.

3.3 Imaging of biological Samples using custom-made SIM

As the primary application of the SIM setup is the imaging of biological samples, we demonstrated the capabilities of our custom-made SIM microscope by imaging fluorescently labelled astrocytes. A laser diode emitting at the wavelength of 488 nm was used for excitation of the fluorescently labelled vimentin filament protein within these cells, [38]. The emission filter (MF530-43, Thorlabs, USA) was used for spectral filtering. Figure 5a, presents the sample recorded in the EPI imaging modality. Subsequently, we recorded a total of nine images, for three different phases at each of three distinct orientations of the diffraction grating. The superresolution SIM image, Figure 5b, was obtained by reconstructing these nine images using the MAP SIM algorithm of the SIMToolbox software. The insets, Figures 5c and 5d, show the same sample region recorded in EPI and SIM imaging modalities, respectively. These insets clearly illustrate the enhanced resolution achieved with SIM imaging. To confirm the resolution improvement, we extracted intensity profiles across the marked region on the insets, for both EPI and SIM images. The intensity profile, Figure 5e, obtained from the superresolution SIM image reveals fine structures of the vimentin cytoskeleton that remain unresolved in the EPI image.

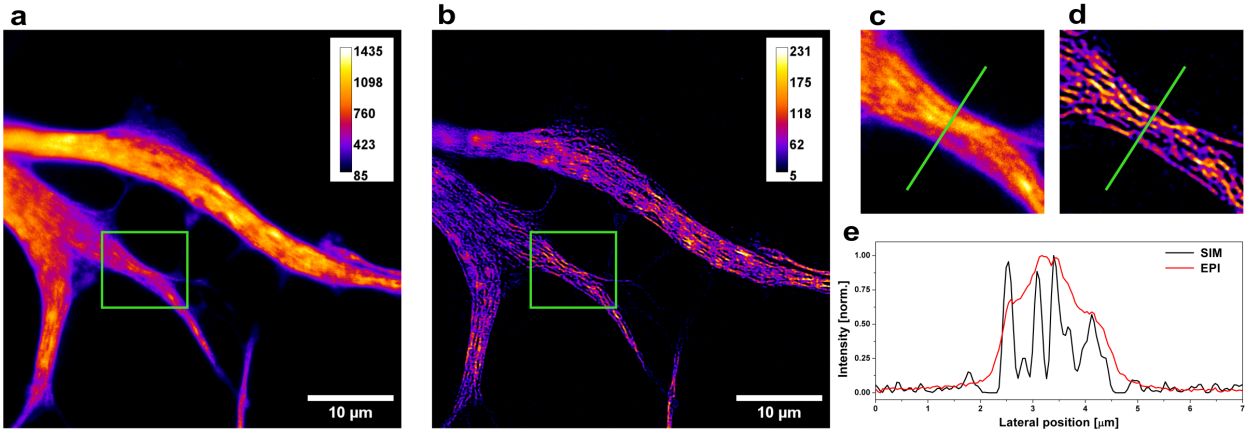

Figure 5: **Superresolution Imagining of fluorescently labelled Astrocytes.** a) The EPI image. b) The superresolution SIM image. The insets show enlarged areas of the sample marked on the EPI image c) and superresolution SIM image d). e) The intensity profiles extracted across the marked areas of the corresponding insets clearly show an improvement in the resolution of SIM over the EPI imaging modality.

4 Conclusion

We have developed a method to fabricate the transmission diffraction gratings suited to the specific requirements of our system. From a variety of gratings produced via microfilming method, we implemented the one providing the finest pattern in the sample plane, characterized by a period of 272 nm. The variation in power distribution between ± 1 orders is approximately 5% or less. The losses associated with the presence of higher diffraction orders (which remain below 20%) arise due to the non-sinusoidal transmission of the grating, a limitation inherent to the analogue microfilming method. We examined the photostability of the produced gratings over a two-year period, which revealed no degradation of the grating over time.

We employed two distinct measurement approaches to evaluate the resolution enhancement achieved by implementing this grating. Initially, we utilized a conventional resolution measurement technique involving the imaging of sub-resolution-sized fluorescent beads. In the EPI modality, the resolution measurement resulted in (243 ± 9) nm. Following the same protocol for the SIM modality, we obtained the resolution of (163 ± 6) nm. For a more accurate resolution measurement, a deconvolution method must be applied, given the anticipated resolution and bead size. Following this, we applied the knife-edge technique on transition metal dichalcogenides, specifically on the sharp edges of MoS_2 monolayer flakes. The obtained resolution in the EPI imaging modality is (212 ± 4) nm. The reconstructed image generated using the MAP-SIM algorithm yielded a mean FWHM value of (134 ± 8) nm, indicating an enhanced resolution compared to EPI imaging. Furthermore, we investigated the resolution of the image reconstructed by the OS-SIM algorithm. The obtained resolution of (153 ± 5) nm corresponds to the maximum expected improvement of 1.4 times relative to the EPI imaging modality.

To conclude, we have successfully developed a method to fabricate transmission diffraction gratings capable of generating fine illumination patterns in the sample plane of our custom-made SIM setup. Moreover, this method allows us to fabricate diffraction gratings with preferred constants, ensuring excellent transmission in both the visible and near-infrared spectra. Consequently, these gratings are well-suited for the development of near-infrared SIM setups. However, the recording using diffraction grating fabricated by the microfilming method is slower compared to SIM setups that utilize SLMs. Nonetheless, the cost-effectiveness of production of these gratings is significantly higher—up to a hundred times—compared to commercial alternatives such as DOE and SLM. We have successfully demonstrated the capabilities of our microscope by imaging fluorescently labelled astrocytes, specifically the vimentin filament protein within these cells. The SIM images reveal fine structures of the vimentin cytoskeleton that remain unresolved in the EPI image.

5 Competing interests

No competing interest is declared.

6 Acknowledgments

The research was supported by the Move For The Science project, granted by Philip Morris. Special thanks to Milan Minić for his invaluable technical assistance and support. Our gratitude is extended to the Laboratory for Biology at the Petnica Research Center for providing a sample of fluorescently labelled astrocytes. We would like to thank prof. Vladana Vukojević from Karolinska Insitute in Stockholm, Sweden for providing fluorescent beads. Additionally, we appreciate the support provided by Lid d.o.o. company for microfilming. The authors acknowledge funding provided by the Institute of Physics Belgrade, through the grant by the Ministry of Education, Science, and Technological Development of the Republic of Serbia.

References

[1] P. Mondal, A. Diaspro, *Fundamentals of Fluorescence Microscopy: Exploring Life with Light*, **2013**, pp. 1–218.

[2] S. Hess, T. Girirajan, M. Mason, *Biophysical journal* **2007**, *91*, 4258–72.

[3] S. Hell, J. Wichmann, *Optics letters* **1994**, *19*, 780–2.

[4] R. Schmidt, T. Weihs, C. Wurm, I. Jansen, J. Rehman, S. Sahl, S. Hell, *Nature Communications* **2021**, *12*, DOI 10.1038/s41467-021-21652-z.

[5] A. Diaspro, M. A. Van Zandvoort, *Super-Resolution imaging in biomedicine*, **2016**.

[6] M. Gustafsson, *Journal of microscopy* **2000**, *198*, 82–7.

[7] R. Heintzmann, T. Huser, *Chemical Reviews* **2017**, *117*, DOI 10.1021/acs.chemrev.7b00218.

[8] Y. Wu, H. Shroff, *Nature Methods* **2018**, *15*, DOI 10.1038/s41592-018-0211-z.

[9] R. Heintzmann, C. Cremer in European Conference on Biomedical Optics, **1999**.

[10] L. Gao, N. Bedard, N. Hagen, R. T. Kester, T. S. Tkaczyk, *Opt. Express* **2011**, *19*, 17439–17452.

[11] L. Wang, M. C. Pitter, M. G. Somekh, *Opt. Lett.* **2011**, *36*, 2794–2796.

[12] M. Gustafsson, L. Shao, P. Carlton, C.-J. Wang, I. Golubovskaya, W. Cande, D. Agard, J. Sedat, *Biophysical journal* **2008**, *94*, 4957–70.

[13] T. Matsuzaki, R. Kawamura, A. Yamamoto, H. Takahashi, M. Fujii, S. Togo, Y. Yoneyama, F. Hakuno, S.-I. Takahashi, M. Suganuma, S. Nakabayashi, S. Sharma, J. Gimzewski, H. Yoshikawa, *The Journal of Physical Chemistry Letters* **2024**, 1097–1104.

[14] G. Liu, N. Xu, H. Yang, Q. Tan, G. Jin, *Photon. Res.* **2022**, *10*, 1317–1324.

[15] R. Förster, H.-W. Lu-Walther, A. Jost, M. Kielhorn, K. Wicker, R. Heintzmann, *Opt. Express* **2014**, *22*, 20663–20677.

[16] D. Dan, B. Yao, M. Lei, *Chinese Science Bulletin* **2014**, *59*, 1291–1307.

[17] G. Calisesi, D. Ancora, C. Tacconi, A. Fantin, P. Perin, R. Pizzala, G. Valentini, A. Farina, A. Bassi, *Microscopy and Microanalysis* **2022**, *28*, 1–10.

[18] S. Hu, L. Liu, Y. Huang, W. Liu, Q. Wei, M. Tan, Y. Yu, *Optics Communications* **2019**, *436*, 227–231.

[19] Ø. Helle, F. Dullo, M. Lahrberg, J.-C. Tinguely, O. Hellesø, B. Ahluwalia, *Nature Photonics* **2020**, *14*, 1–8.

[20] M. Calvarese, P. Paiè, A. Candeo, G. Calisesi, F. Ceccarelli, G. Valentini, R. Osellame, H. Gong, M. Neil, F. Bragheri, A. Bassi, *Opt. Express* **2022**, *30*, 30246–30259.

[21] M. Müller, V. Mönkemöller, S. Hennig, W. Hübner, T. Huser, *Nature communications* **2016**, *7*, 10980.

[22] P. Křížek, T. Lukes, M. Ovesny, K. Fliegel, G. Hagen, *Bioinformatics (Oxford England)* **2015**, *32*, DOI 10.1093/bioinformatics/btv576.

[23] J. Pospisil, T. Lukes, J. Bendesky, K. Fliegel, K. Spendier, G. Hagen, *GigaScience* **2018**, *8*, DOI 10.1093/gigascience/giy126.

[24] M. Ingaramo, A. York, E. Hoogendoorn, M. Postma, H. Shroff, G. Patterson, *Chemphyschem : a European journal of chemical physics and physical chemistry* **2014**, *15*, DOI 10.1002/cphc.201300831.

[25] F. Ströhl, C. Kaminski, *Methods and Applications in Fluorescence* **2015**, *3*, DOI 10.1088/2050-6120/3/1/014002.

[26] M. Schropp, C. Seebacher, R. Uhl, *Photonics* **2017**, *4*, DOI 10.3390/photonics4020033.

[27] M. Schropp, R. Uhl, *Journal of microscopy* **2014**, *256*, DOI 10.1111/jmi.12154.

[28] The SIMToolbox project, https://simtoolbox.github.io/.

[29] D. P. G. Nilsson, T. Dahlberg, M. Andersson, *Appl. Opt.* **2021**, *60*, 3764–3771.

[30] D. Karadaglić, T. Wilson, *Micron* **2008**, *39*, 808–818.

[31] C. R. Minton, *Handbook of Microfilm Technology and Procedures*, Association of Records Managers Administrators (ARMA), **1994**.

[32] J. Park, N. Choudhary, J. Smith, G. Lee, M. Kim, W. Choi, *Applied Physics Letters* **2015**, *106*, 012104.

[33] M. Mylonakis, G. J. Tserevelakis, G. Vlachos, E. Fanouraki, A. Pavlopoulos, M. Pavlidis, G. Zacharakis, *Opt. Lett.* **2024**, *49*, 462–465.

[34] J. Pawley, *Handbook of biological confocal microscopy*, *Vol. 236*, Springer Science & Business Media, **2006**, pp. 59–79.

[35] A. Senkić, J. Bajo, A. Supina, B. Radatović, N. Vujicic, *Materials Chemistry and Physics* **2023**, *296*, 127185.

[36] Y. Zeng, X. Li, W. Chen, J. Liao, J. Lou, Q. Chen, *Advanced Materials Interfaces* **2017**, *4*, DOI 10.1002/admi.201700739.

[37] M. T. Hannebelle, E. Raeth, S. M. Leitao, T. Lukeš, J. Pospíšil, C. Toniolo, O. F. Venzin, A. Chrisnandy, P. P. Swain, N. Ronceray, M. P. Lütolf, A. C. Oates, G. M. Hagen, T. Lasser, A. Radenovic, J. D. McKinney, G. E. Fantner, *bioRxiv* **2023**, DOI 10.1101/2023.06.16.545316.

[38] H. Wu, Y. Shen, S. Sivagurunathan, M. S. Weber, S. A. Adam, J. H. Shin, J. J. Fredberg, O. Medalia, R. Goldman, D. A. Weitz, *Proceedings of the National Academy of Sciences* **2022**, *119*, e2115217119.